Joint Effects of Virtual Surfaces on Anti-icing and Drag Reduction

Yijun Lu *
Beijing Institute of Technology, Beijing 100081, People's Republic of China

Qiangqiang Sun † and Kwing-So Choi ‡
University of Nottingham, Nottingham, NG7 2RD, United Kingdom

Xin Zhang §
China Aerodynamics Research and Development Center, Mianyang 621000, People's Republic of China

Xuerui Mao ¶
Beijing Institute of Technology, Beijing 100081, People's Republic of China

The operation of the anti-icing system of an airplane can modulate its aerodynamics, whilst an aerodynamic control can alter the icing condition. Therefore, one well-designed control strategy can be expected to yield two benefits, which, however, has not been actively investigated. In this work, the constant leading edge blowing technique is deployed to achieve joint effects on anti-icing and drag reduction, first on an airfoil and then on a half-airplane model. The results indicate that dual virtual surfaces (an inner one and an outer one) wrapping the leading edge are generated by the blowing control. The inner one prevents water droplets from impacting and accumulating on the airfoil by changing their trajectories. The outer one redirects the shear generated by the blowing and promotes its rolling up and vortex shedding, generating low pressure zones around the upper leading edge and subsequently reducing drag significantly.

Nomenclature

A = blowing jet amplitude

C_D = drag coefficient

C_{Dp} = pressure drag coefficient

C_{Db} = momentum drag coefficient

C_{Dv} = frictional drag coefficient

C_{D0} = drag coefficient of the baseline (uncontrolled) case

*Graduate Student, School of Aerospace Engineering.
†Research Associate, Faculty of Engineering; sh1225128@sina.com (Corresponding Author).
‡Professor, Faculty of Engineering. Associate Fellow AIAA.
§Associate Professor, State Key Laboratory of Aerodynamics.
¶Professor, Advanced Research Institute of Multidisciplinary Sciences; maoxuerui@sina.com (Corresponding Author).

C_L = lift coefficient

C_{L0} = lift coefficient of the baseline (uncontrolled) case

C_p = pressure coefficient

C_v = local skin friction coefficient

C_μ = blowing jet momentum coefficient

c = chord, m

f_d = water volume fraction

F_r = Froude number

$\boldsymbol{g}$ = gravitational acceleration, m/s^2

h = blowing width, m

LWC = liquid water content in air, g/m^3

MVD = median volumetric diameter of water droplets, μm

P_b = power required to generate the blowing control, W

p_b = local static pressure of the blowing slit, Pa

p_∞ = pressure of freestream, Pa

Re = Reynolds number

$\boldsymbol{u_b}$ = blowing velocity vector, m/s

$\boldsymbol{u_d}$ = droplets velocity vector, m/s

u_x = mean streamwise velocity, m/s

u_∞ = freestream velocity, m/s

α = angle of attack, $^\circ$

τ_ω = wall shear stress, N/m^2

I. Introduction

Icing on the surface of an airplane, especially on the leading edge of the wing, has been notorious for leading to flight catastrophes. In icing conditions, the water droplets in the clouds impact the airplane surface, resulting in degradation of the aerodynamic performance and malfunction of essential instruments. It has been demonstrated in experiments that a layer of 1 mm ice accumulating on the leading edge or upper surface of the wing can cause a reduction in lift of over 30% and an increase in drag of over 50% [1]. Therefore, extensive research has been devoted to developing anti-/de-icing techniques and revealing the underlying physical mechanisms [2–5].

Conventional (i.e., mechanical, thermal, and chemical liquid) anti-/de-icing techniques have various drawbacks, such as high energy consumption, complex mechanical structures, and deterioration of aerodynamic performances.

For example, the pneumatic ice removal system is widely used in relatively small airplanes, and it alters the airplane's aerodynamic shape and increases drag as pneumatically inflated rubber boots on the leading edge of the wing expand during operation [6]. Similarly, in icing conditions, severe separation of the airflow behind the ice ridges that form outside the anti-icing area can lead to decrement in the lift-to-drag ratio if the energy supply of the hot air anti-icing system is insufficient [7]. Additional active flow control techniques are usually required to compensate the loss of aerodynamic performances caused by these methods, resulting in redundancy of control systems.

In recent years, various novel methods have been developed to address anti-/de-icing. To name a few, Nagapan et al. [8, 9] used an array of thermally activated synthetic jet actuators embedded in the ice accumulation region of an airplane surface to achieve anti-/de-icing efficiently. Also, an anti-icing method based on the dielectric barrier discharge plasma actuators was presented by Zhou et al. [10], and the aerodynamic and thermal effects were found to be the main mechanisms for anti-/de-icing. Then, Yang et al. [11] proposed a hybrid anti-icing method combining thermoelectric systems and synthetic jet actuators. Although these anti-/de-icing techniques are mainly realized by various control systems, their effects on aerodynamic forces have not been actively discussed. In a broad view, the controls of icing and aerodynamics are naturally coupled, and one strategy would receive conflicting or co-benefiting effects.

In this work, a well-tested flow control technique, namely, leading-edge blowing, is studied to explore its joint effects on aerodynamics and anti-/de-icing. The concept, parameter dependence, and mechanism are first revealed in an airfoil case and then extended to a half-airplane model. It is illustrated for the first time that the blowing control achieves anti-icing effects by creating dual virtual surfaces, preventing the droplets from reaching the airfoil surface. In the following, the numerical algorithms to simulate the airflow and the impact characteristics of water droplets are outlined in Section II. The computational setup and theoretical formulations for the joint control are presented in Section III, followed by extensive validations in Section IV. The effects of joint control, as well as the mechanisms underpinning anti-icing and drag reduction, and the demonstration of these effects in engineering applications are presented in Section V. Finally, conclusions are drawn in Section VI.

II. Methodology

The incompressible Navier-Stokes equations are used as the governing equations, and large eddy simulation (LES) is adopted:

$$\frac{\partial \bar{u}_i}{\partial x_i} = 0, \ \frac{\partial \bar{u}_i}{\partial t} + \frac{\partial}{\partial x_j}(\bar{u}_i \bar{u}_j) = -\frac{1}{\rho}\frac{\partial \bar{p}}{\partial x_i} + \frac{\partial}{\partial x_j} \times \left[v \left(\frac{\partial \bar{u}_i}{\partial x_j} + \frac{\partial \bar{u}_j}{\partial x_i} - \frac{2}{3}\delta_{ij}\frac{\partial \bar{u}_k}{\partial x_k} \right) \right] - \frac{\partial \tau_{ij}^{SGS}}{\partial x_j}, \tag{1}$$

where the components of the velocity vector in x_i, x_j and x_k coordinate directions are given by u_i, u_j and u_k, respectively, ρ is the density, p is the pressure, v is the kinematic viscosity, δ is the Dirac delta function, $\bar{\cdot}$ is the spatial filtering

operator, and τ_{ij}^{SGS} is the subgrid-scale stress given by

$$\tau_{ij}^{SGS} = \overline{u_i u_j} - \bar{u}_i \bar{u}_j, \tag{2}$$

The eddy-viscosity is supposed as follows:

$$\tau_{ij}^{SGS} - \frac{1}{3}\tau_{kk}\delta_{ij} = -2\mu_t \bar{S}_{ij}, \text{ with } \bar{S}_{ij} = \frac{1}{2}\left(\frac{\partial \bar{u}_i}{\partial x_j} + \frac{\partial \bar{u}_j}{\partial x_i}\right), \tag{3}$$

where μ_t is the subgrid-scale turbulent viscosity, and S_{ij} is the rate-of-strain tensor.

An algebraic Wall-Modeled LES model [12] is adopted to solve the eddy viscosity μ_t. The pressure velocity coupling is achieved using a numerical scheme based on the SIMPLEC algorithm [13]. The finite volume discretization of a bounded central differencing scheme is used for momentum discretization, while a bounded second-order implicit scheme is adopted for temporal discretization [14]. To ensure the full development of the flow field, the steady-state solution calculated by the k$-\omega-$SST model was used as the initial condition of the flow field [15].

The force acting on the surface of the airfoil is defined as [16]:

$$\boldsymbol{f} = \int_C \left(p\boldsymbol{n} - Re^{-1}\partial_n \boldsymbol{u} + \boldsymbol{u_b}\boldsymbol{u_b} \cdot \boldsymbol{n}\right) \mathrm{d}\boldsymbol{C}, \tag{4}$$

where $\boldsymbol{u} = \left(u_i, u_j, u_k\right)^T$, $\boldsymbol{u_b}$ is the blowing velocity on the surface, and $\boldsymbol{n}$ is the wall-normal unit vector of the airfoil. The three terms integrated on the right-hand side in Equation (4) denote the pressure, viscous, and blowing forces, respectively. Clearly, it becomes the uncontrolled case at $\boldsymbol{u_b} = 0$. Then, the lift and drag coefficients denoted as C_L and C_D can be obtained by projecting $\boldsymbol{f}$ to the streamwise and normal directions respectively, and divided by $0.5\rho u_\infty^2 bc$, where u_∞ is the velocity of freestream, b is the spanwise length of the airfoil and c is the chord length, and they can be further decomposed as:

$$C_L = C_{Lp} + C_{Lv} + C_{Lb},\ C_D = C_{Dp} + C_{Dv} + C_{Db}, \tag{5}$$

where the subscripts p, v, or b are the terms contributed by pressure, viscous, and blowing forces, respectively.

The fluid physics of the control effect can be examined by studying the distribution of the pressure coefficient C_p and the skin friction coefficient C_v, defined as:

$$C_p = \frac{p - p_\infty}{0.5\rho u_\infty^2},\ C_v = \frac{\tau_\omega}{0.5\rho u_\infty^2}, \tag{6}$$

where p_∞ is the pressure of freestream and τ_ω is the wall shear stress.

Both Lagrange and Euler methods have been utilized to investigate the impact characteristics of water droplets on

the airfoil surface. In the Lagrange one, the water droplets are considered as particles affected by airflow. The trajectory of water droplets obtained through solving the kinematic equations is deployed to determine the impact characteristics and the local water droplet collection coefficient (it represents the impact range and distribution of water droplets on the surface) [17]. Moreover, one should note that, in the Lagrange method, the trajectory of each water droplet has to be solved individually, which leads to almost unaffordable computational costs, especially for the three-dimensional simulations. In contrast, water droplets are regarded as a continuously distributed medium resembling the airflow in the Euler method. The spatial distribution and other quantities (i.e., velocity and local water droplet collection coefficient) of water droplets are then computed using the identical method as solving the airflow field [18]. Therefore, the impact characteristics of water droplets are systematically analyzed based on the Euler method in the current work, wherein water droplets satisfy the conservation of mass and momentum:

$$\frac{\partial f_d}{\partial t} + \nabla \cdot (f_d \boldsymbol{u_d}) = 0, \ \frac{\partial \boldsymbol{u_d}}{\partial t} + \boldsymbol{u_d} \cdot \nabla \boldsymbol{u_d} = \frac{C_d Re_d}{24K} (\boldsymbol{u} - \boldsymbol{u_d}) + \left(1 - \frac{\rho}{\rho_d}\right) \frac{1}{Fr^2} \boldsymbol{g}, \tag{7}$$

where ρ_d is the droplets density, f_d is the volume fraction of droplets, $\boldsymbol{u_d}$ denotes the droplets velocity, Re_d is the droplets Reynolds number, $C_d = (24/Re_d)\left(1 + 0.15Re_d^{0.687}\right)$ for $Re_d \leq 1000$ and $C_d = 0.4$ for $Re_d > 1000$ is the drag coefficient for droplets [19], K is an inertia parameter, Fr is the Froude number, and $\boldsymbol{g}$ is the gravitational acceleration.

III. Numerical Setup

A. NACA0012 Airfoil

As an initial study, the NACA0012 airfoil with a chord length of 0.5 m and spanwise length of 0.1 m with periodic spanwise boundary conditions is used to test the proposed method. The computational domain is shown in Fig.1, and the non-dimensional wall distance of the first mesh layer remains $y^+ \leq 1$ on the entire surface. The density (ρ), viscosity (μ), and angle of attack (α) of the inflow are 1.317 kg/m^3, $1.691 \times 10^{-5} kg/(m \cdot s)$ and 2°, respectively. The freestream velocity (u_∞) varies from 10 to 50 m/s corresponding to Reynolds number (Re) based on the freestream velocity and chord length from 3.89×10^5 to 1.94×10^6. A total of 26,709,600 cells are generated with a significant concentration around the leading edge.

A blowing slit near the leading edge is created as sketched in Fig.1(b). This slit does not vary in the spanwise direction and its streamwise length ranges from 3.8% to 6.25% of c from case to case. The magnitude of the control $\|\boldsymbol{u_b}\|$ ranges from 25% to 30% of u_∞ and its direction is perpendicular to the airfoil surface. This form of control is generally characterized by a non-dimensional momentum coefficient (C_μ) describing the non-dimensional force due to the added momentum to the flow [20–22]:

$$C_\mu = \frac{\rho b h \|\boldsymbol{u_b}\|^2}{\rho b c u_\infty^2} = \frac{h}{c} A^2, \text{ with } A = \frac{\|\boldsymbol{u_b}\|}{u_\infty}, \tag{8}$$

where h is the blowing slit width and A is the blowing amplitude. Throughout this work, C_μ and A are employed to evaluate the effectiveness of joint control on both anti-icing performance and aerodynamic characteristics of the airfoil.

B. High Lift Common Research Model

The Common Research Model (CRM) in high-lift condition is chosen to demonstrate the effectiveness of the proposed method in an engineering scenario. CRM, a publicly available geometry [23], is designed to epitomize contemporary civil transport jets. The high-lift version of this geometry [24] embodies the landing configuration and has been computationally studied in various AIAA high-lift workshops. Subsequently, the High Lift Common Research Model (HL-CRM) with a mean aerodynamic chord of 7 m from the 4th AIAA CFD high-lift prediction workshop (HLPW-4) [25] is then employed to evaluate the efficacy of the joint control in a more applied sense. The angle of attack and Reynolds number based on the mean aerodynamic chord and freestream velocity are 7° and 5.49×10^6, respectively. The static pressure (p) is configured as 170,093 Pa to ensure that the simulation case aligns with the wind tunnel experiment provided in the 4th AIAA CFD high-lift prediction workshop (HLPW-4) [26]. The computational grid with a total of 21,868,681 cells is generated, and the part around the model is shown in Fig.2. (This grid is publicly available on the HLPW-4 website [25].)

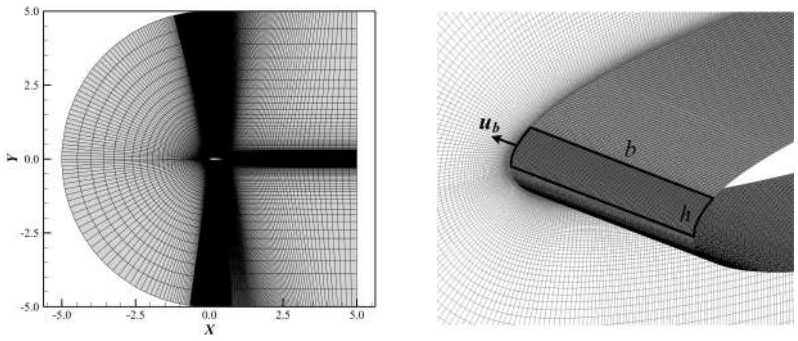

(a) Global mesh in the x-y plane (b) Local mesh near the leading edge

Fig. 1 (a) and (b) : overall and local mesh for flow around NACA0012, respectively.

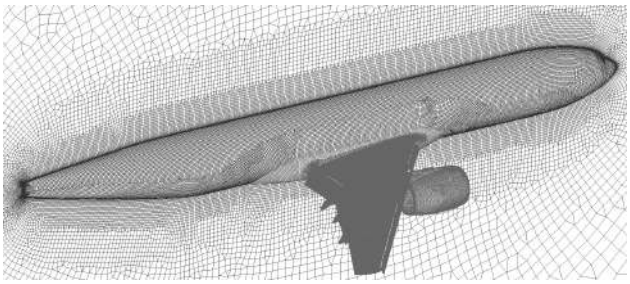

Fig. 2 Computational grids around the HL-CRM.

IV. Validation

In this section, three quantities, including the lift coefficient and water droplet collection efficiency of the NACA0012 airfoil, and the pressure coefficient of HL-CRM, are computed and averaged over ten periods to validate the accuracy of the numerical simulation.

A. Lift Coefficient

Figure.3 shows the comparison of the lift coefficient obtained in the current work with references [27–30] for the NACA0012 airfoil at $Re = 1 \times 10^6$ and $\alpha = 0 \sim 12°$. It is clear that the present data is in good agreement with published experimental and numerical results [27–30].

B. Local Collection Efficiency

Then, the local collection efficiency of droplet around the NACA0012 airfoil with $c = 0.5334\ m$ is computed and compared with the reference [31]. It can be seen from Fig.4 that the impingement thresholds and peak values obtained in this work coincide with those reported in previous efforts [31]. The parameter S represents the distance from the stagnation point x_0 where the local collection efficiency of droplet reaches the maximum value. Moreover, one can observe that the local collection efficiency peaking at the stagnation point decreases rapidly downstream.

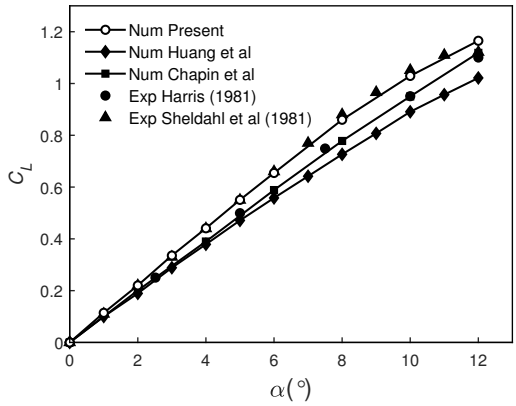

Fig. 3 Comparison of the computed lift coefficient of the NACA0012 airfoil with the published ones at $\alpha = 0 \sim 12°$ and $Re = 1 \times 10^6$ (Num and Exp represent numerical and experimental data, respectively).

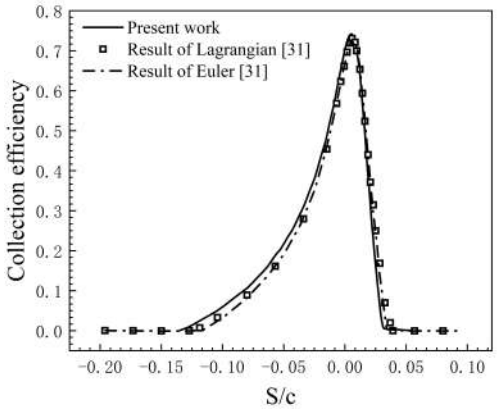

Fig. 4 The distribution of the droplet collection efficiency in flow around NACA0012 at $\|u_d\| = 112\ m/s$, $\alpha = 7°$, $LWC = 1\ g/m^3$, and $MVD = 20\ \mu m$ ($S/c = 0$ corresponds to the stagnation point).

C. Pressure Coefficient of The HL-CRM

Flow over the HL-CRM is considered as another case to further validate the accuracy of the applied numerical method. A slice F illustrated in Fig.5(a) showing the distribution of the pressure coefficient over the surface of the HL-CRM is extracted, and the corresponding pressure coefficient is shown in Fig.5(b~d). There are considerable

differences between present CFD results and the experimentally measured local pressure [25], which might be attributed to the noise associated with individual pressure sensors. After integrating over the surface, the simulated aerodynamic force agrees with the experimental one well, as shown in Table 1.

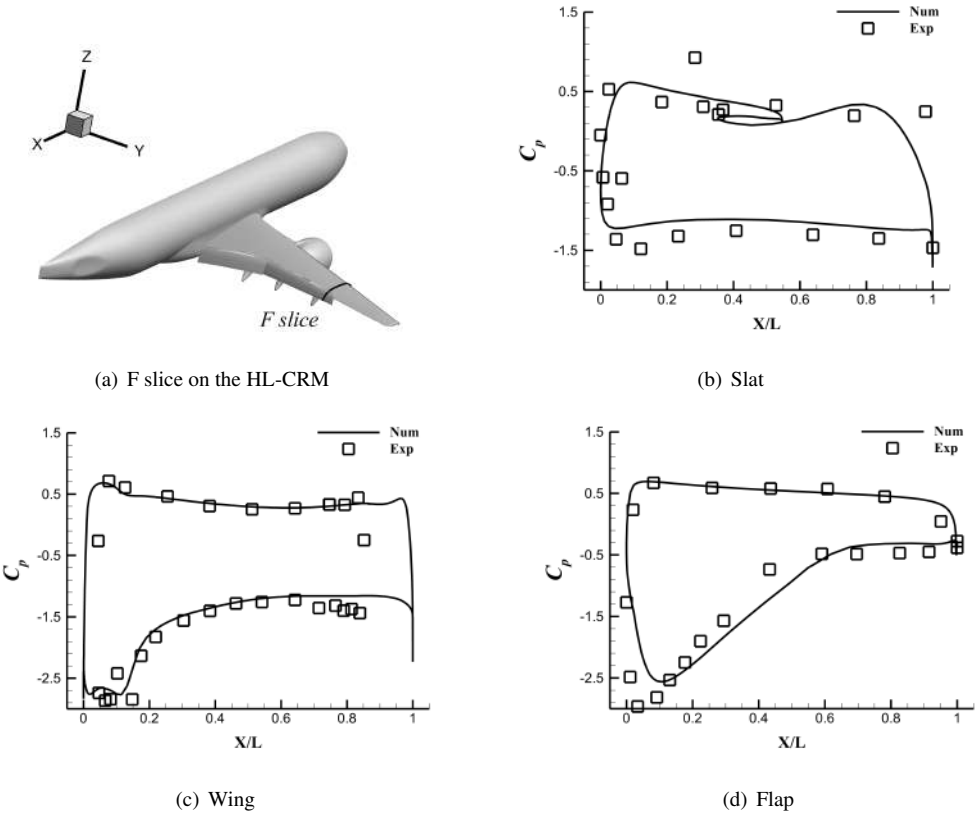

(a) F slice on the HL-CRM (b) Slat

(c) Wing (d) Flap

Fig. 5 Distributions of the pressure coefficient of (a) F slice ($y = 20.1\ m$) on the HL-CRM at (b) slat, (c) wing and (d) flap (Num and Exp represent numerical and experimental data, respectively; X=0 represents the position of the leading edge of the slat/wing/flap).

Table 1 Validation results of lift and drag coefficients on the HL-CRM

CASE	C_L	C_D
Experiment Data [25]	1.7786	0.1867
Present Work	1.7076	0.1895

V. Results

After validating the employed numerical methodology, the influences of control parameters such as the blowing width h and amplitude A on aerodynamic performances (i.e., lift and drag coefficients), as well as water droplets impingement characteristics are investigated in Section A, followed by the analyses of mechanisms on anti-icing and drag

reduction in Section B and C, respectively. The effectiveness of the proposed method in a more engineering-relevant example, i.e., the HL-CRM, is then demonstrated in Section D.

A. Control Effect on Icing and Aerodynamic Forces

The aerodynamic characteristics of the NACA0012 airfoil are investigated across a range of freestream velocities ($u_\infty = 10, 26, 40, 50\ m/s$). The dependencies of lift and drag coefficients normalized by the uncontrolled value on the blowing amplitude A are depicted in Fig.6(a) and (b), respectively. The blowing width is the optimized value that will be discussed later with Fig.8(a). One can observe a discernible downward trend in the lift, which is consistent with the effect of leading-edge blowing on lift performances in a previous study [27]. A strong downward trend is observed for the drag coefficient, and the underlying mechanism will be discussed later in Section C. However, in the case $u_\infty = 26\ m/s$, the lift coefficient is almost invariant (within 2% error) despite changes in the blowing amplitude, while the drag reduction progressively increases with A and reaches 87%. In the following investigations of the airfoil flow, the freestream velocity will be fixed at 26 m/s so as to concentrate on the effects of the control parameters.

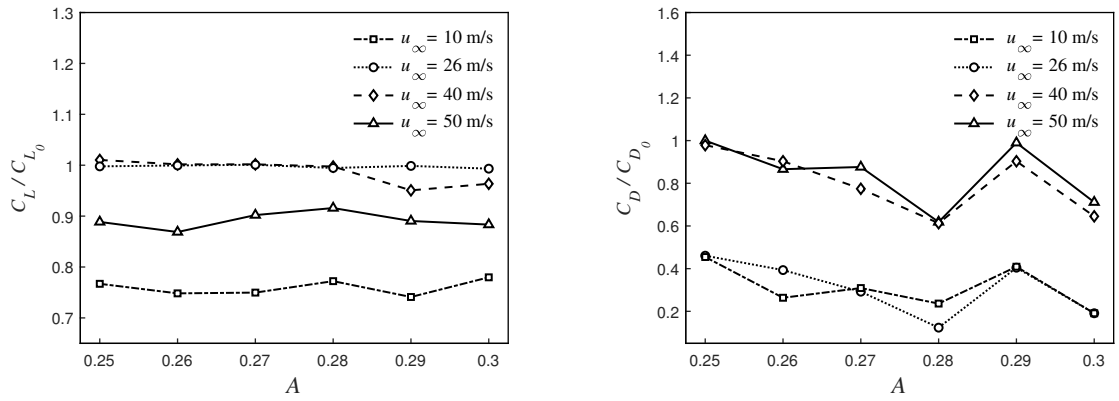

(a) Lift coefficient vs A

(b) Drag coefficient vs A

Fig. 6 Effects of the blowing amplitude A on (a) the lift and (b) drag coefficients of the NACA0012 airfoil. The corresponding blowing width is determined by the optimal control schemes at $u_\infty = 26\ m/s$, as will be illustrated in Fig.8(a).

The behavior of droplets, including their collection efficiencies and impact characteristics, is crucial in determining the resulting ice shape on the airfoil surface. As such, the current work focuses on the changes in the water droplets' trajectories caused by the constant blowing flow control. As illustrated in Fig.7(a), water droplets predominantly accumulate near the leading edge rather than on the upper/lower surface of the airfoil. This poses a significant challenge as it would freeze into ice and then disrupt the airflow in icing conditions, resulting in undesirable aerodynamic effects, such as increased drag and reduced lift. However, by imposing blowing control within a small region, icing around the leading edge can be effectively eliminated, as evidenced by Fig.7(b). This is because the blowing control redistributes

the water droplets and prevents their accumulation at the critical leading edge region. Moreover, although limited water droplets adhere to the upper surface of the airfoil due to the separation bubble downstream of the blowing jet and form a very thin water film, they do not lead to significant icing hazards as the aerodynamics is not sensitive to geometry changes in this region [16]. As a result, the icing problem can be considered to be eliminated by avoiding the impingement of water droplets on the leading edge of the airfoil.

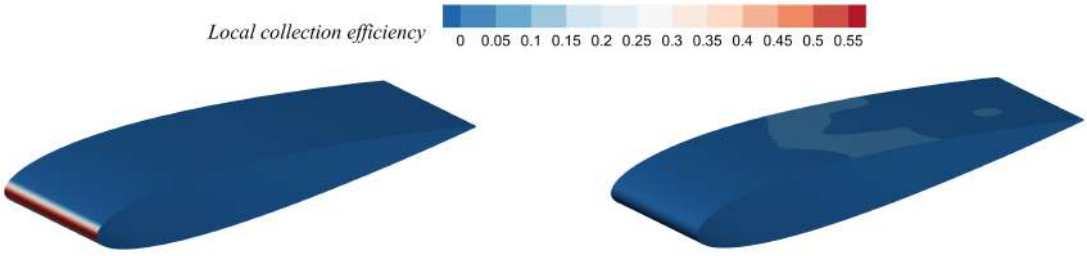

(a) Control off (b) Control on

Fig. 7 Water droplet collection efficiency of the NACA0012 for the (a) control-off and (b) control-on cases at $u_\infty = 26\ m/s$, $A = 0.30$, $h = 5.25\%c$.

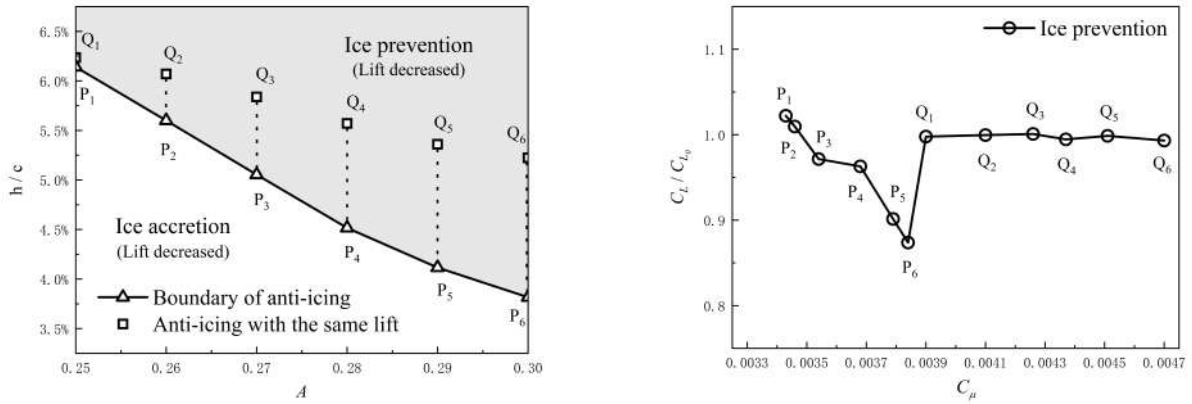

(a) Width of blowing jet vs A (b) Lift coefficient vs C_μ

Fig. 8 Effects of the blowing jet amplitude and width on (a) anti-icing and (b) lift coefficient at different blowing momentum coefficients in the NACA0012 flow at $u_\infty = 26\ m/s$.

Effective anti-icing capability can be obtained by optimizing the blowing velocity and width, as delineated by the shadow region in Fig.8(a) for the case of $u_\infty = 26\ m/s$. The control schemes can be classified into two distinct groups based on whether they can suppress the ice formation, with P_1 to P_6 representing the boundary between these categories. It should be noted that, from P_1 to P_6, the lift is observed to attenuate progressively with the increasing of blowing amplitude (see Fig.8(b)). To ensure that the lift does not reduce significantly, the blowing width is further optimized, and the corresponding results (namely, Q_1 to Q_6) are also shown in Fig.8(a). With these optimized control parameters, the lift coefficient closely approximates that of the baseline case (within 2% error, see Fig.8(b)), while the drag coefficient

can be attenuated by up to 87%, as shown in Table 2. This elucidates that, by varying the blowing width and amplitude, the joint control of anti-icing and drag reduction can be achieved without compromising the lift performance. In the following of this work, the case $A = 0.30$ and $h = 5.25\%c$ where the additional power $P_b=(p_b-p_\infty)\|\boldsymbol{u_b}\|bh$ [32] required to generate the blowing control is 8.29 W will be adopted unless otherwise stated.

B. Anti-icing Mechanism

In this section, the mechanism of anti-icing observed in section A is revealed by examining the interaction between water droplets and the surrounding airflow. Figure.9(a) and (b) describe the distribution and trajectory of water droplets on the airfoil surface with/without the blowing control. When the control is off, water droplets predominantly accumulate along the suction side of the leading edge due to surface adhesion before eventually dispersing downstream [18]. However, a long and narrow sheltered region, characterized by no droplets near the airfoil surface, expands on both sides of the airfoil and even envelops the entire airfoil when imposing the blowing control. Therefore, the blowing jet facilitates the expulsion of water droplets away from the airfoil, thereby disrupting the potential formation and accumulation of ice.

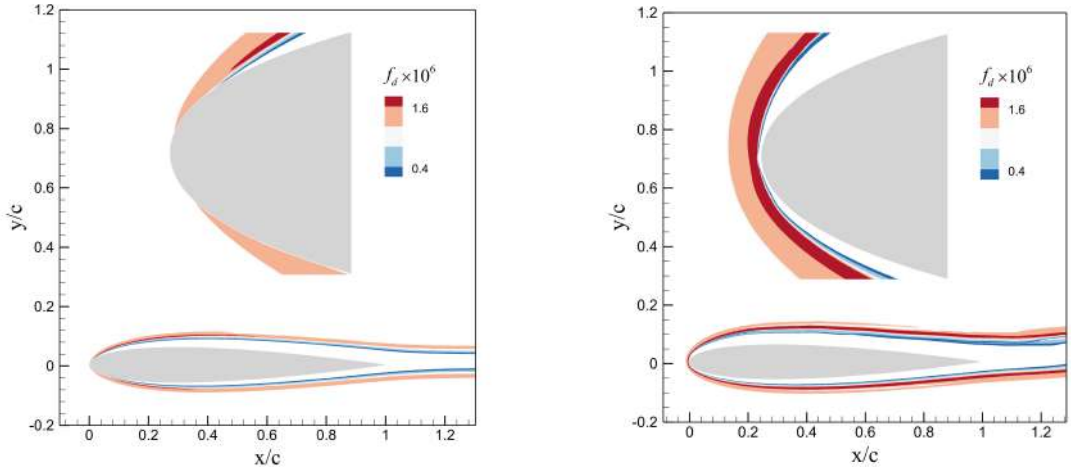

(a) Control off (b) Control on

Fig. 9 Distribution of the water volume fraction on the surface of NACA0012 for the (a) control-off and (b) control-on cases.

As depicted in Fig.10, the dashed lines are streamlines, whereas the solid ones mark the incoming water droplets trajectories. When the jet flow interacts with the main flow, a "bubble" (see the light blue region) is generated upstream of the leading edge, and its outer boundary forms a virtual airflow surface, i.e., the outer one. Owing to the interaction between water droplets and the blowing jet, a smaller "bubble" indicative of a region impeding water droplets movement is discerned within the dark blue region, and its outer boundary represents a virtual surface of water droplets, i.e., the inner one. It can be seen from Fig.10 that even if water droplets penetrate the first "bubble", they cannot traverse the

second one, which functions as a barrier to impede the collision of water droplets with the airfoil surface. Therefore, this dynamic process, characterized by the creation of virtual surfaces through the blowing jet, effectively modifies the trajectories of water droplets. By altering the distribution of droplet collection rates on the airfoil surface, the joint control ensures that the airfoil surface remains free from water droplets, achieving anti-icing effects.

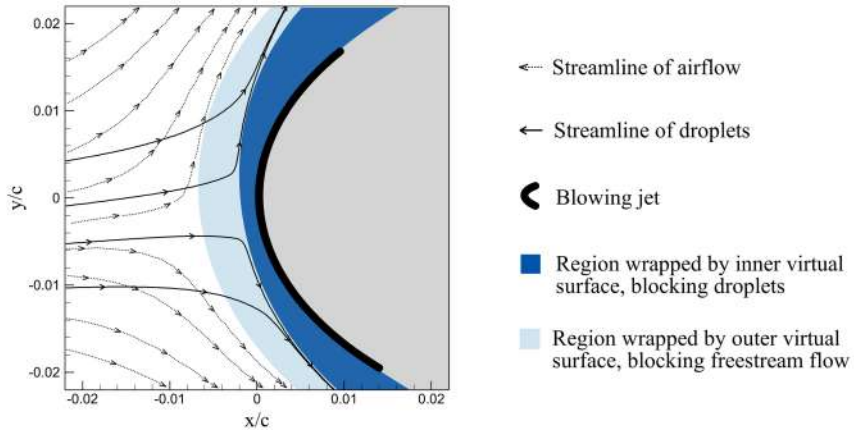

Fig. 10 The schematic of dual virtual surfaces created by the blowing control.

C. Drag Reduction Mechanism

In this section, the mechanism of drag reduction is revealed by examining the components of aerodynamic forces and the flow field. The time-averaged pressure coefficient distribution over the suction/pressure surface of the airfoil is shown in Fig.11(a). For the controlled cases, a low pressure region is observed at $x/c = 0 \sim 0.3$ where the pressure coefficient is almost invariant. Also, the skin friction exhibits small variations immediately downstream of the controlled region. This effect can be attributed to the introduction of a local pressure jump at the onset of the control, as also observed in the flat-plate turbulent boundary layers [33]. Downstream of this region, pressure recovers gradually before the flow separates at $x/c \approx 0.22$ and reattaches at $x/c \approx 0.38$ in Fig.11(b). Clearly, over this separation zone, the skin friction coefficient is negative.

For the uncontrolled case, it can be seen from Fig.12(a) that the flow development is normal. Two-dimensional structures related with Tollmien-Schlichting (T-S) waves are generated downstream of the leading edge. These waves are subject to instabilities and develop into three-dimensional Λ structures with a clear spanwise wavenumber, whose breakdown finally completes the transition to turbulence. Interestingly, the control promotes separation and moves the transition point upstream, as illustrated in Fig.12(b). The separated shear layer rolls up, evolves into spanwise vortical structures and then loses stability manifesting three-dimensional structures. Further downstream, hairpin vortices well observed in boundary layer flow appear [34]. These shedding vortices are associated with low pressure and subsequently reduce the pressure on the suction side of the airfoil and contribute to the reduction of pressure drag. In this process, the two-dimensional base flow supporting the growth of TS waves is broken, and therefore, these waves are not observed in

the controlled case.

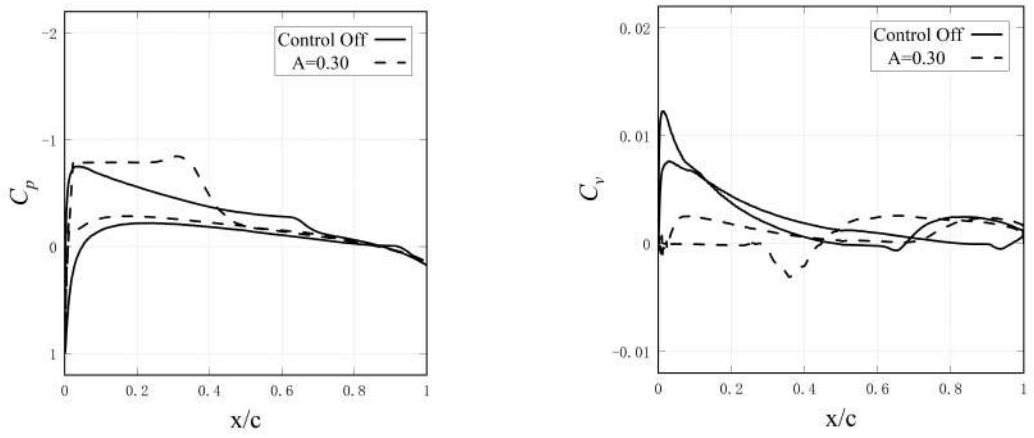

(a) Pressure coefficient (b) Skin friction coefficient

Fig. 11 Distribution of time-averaged (a) pressure coefficient and (b) skin friction coefficient on the NACA0012 airfoil surface with or without blowing control.

This drag reduction mechanism is closely associated with the virtual surface between the jet and the freestream. As shown in Fig.13(a), the outer virtual surface redirects the blowing-induced shear, which is analogous to the separated shear layer at high angles of attack and is subject to instabilities and vortex shedding. The consequence is the generation of a low pressure zone (see Fig.13(b)) and drag reduction. Similar mechanisms have been reported in other studies [35, 36].

This reduction of pressure drag is one order higher than the reduction of the viscous drag and the momentum drag, as evidenced by the data presented in Table 2. It is worth noting that despite the flow transition point being much closer to the leading edge in the controlled case, the corresponding lift coefficient is approximately the same value as the baseline.

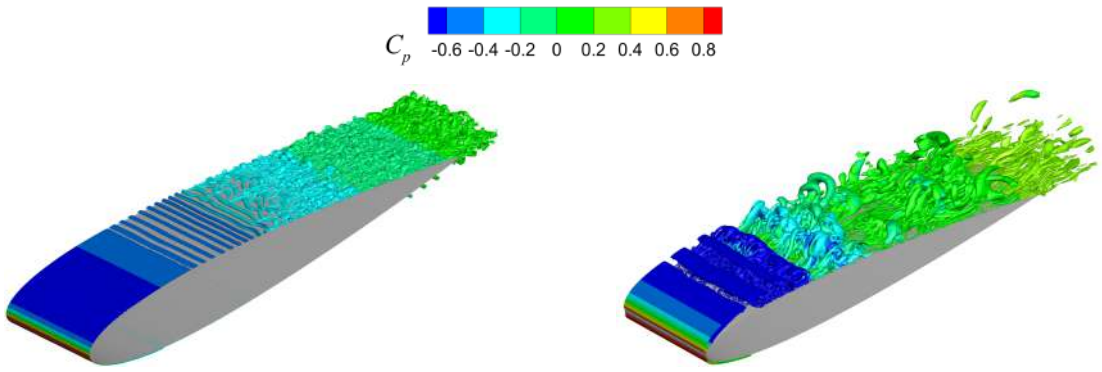

(a) Control off (b) Control on

Fig. 12 Isosurfaces of Q=300,000 colored by pressure coefficient for the (a) control-off and (b) control-on cases.

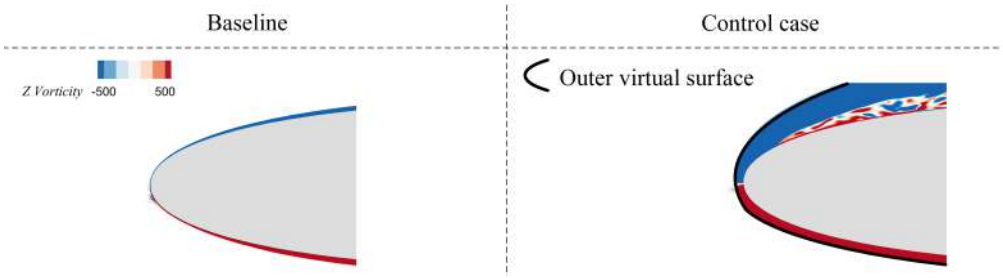

(a) Vortex shedding

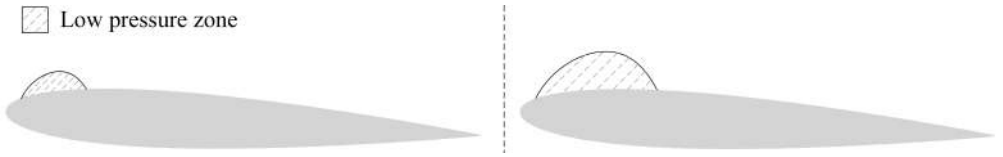

(b) Pressure distribution

Fig. 13 (a) Spanwise vorticity contours around the leading edge, showing the redirection of the blowing flow. (b) The resultant low pressure zone.

Table 2 Analysis of drag coefficient of NACA0012 with or without control

	$C_\mu = 0$	$C_\mu = 0.0039$	$C_\mu = 0.0041$	$C_\mu = 0.0043$	$C_\mu = 0.0044$	$C_\mu = 0.0045$	$C_\mu = 0.0047$
C_{Dp}	0.0039	-0.0018	-0.0028	-0.0040	-0.0057	-0.0036	-0.0058
C_{Dv}	0.0050	0.0017	0.0018	0.0019	0.0019	0.0019	0.0020
C_{Db}	0	0.0042	0.0045	0.0047	0.0049	0.0053	0.0055
C_D	0.0089	0.0041	0.0035	0.0026	0.0011	0.0036	0.0017

After discussing the pressure distribution, we shift our focus to the shear stress on the pressure side of the airfoil. Figure.14(a), (b) and (c) depict the distribution of mean streamwise velocity u_x/U_e, where U_e represents the velocity at the edge of boundary layer, as determined by a diagnostic plots-derived method [37]. After imposing the blowing control, the velocity gradient $(du_x/dy)_w$ on the airfoil surface reduces compared with that for the baseline case, resulting in the reduction of the local frictional factor. Notably, a discernible shift-up in the velocity profile towards the downstream direction is observed. This is likely a consequence of the increased boundary layer thickness, which persists downstream the control region [33, 38]. The thickening of boundary layer suggests the reduction of the skin friction on the pressure surface of the airfoil after imposing the blowing control near the leading edge, as illustrated in Fig.11(b).

For conventional studies without active flow control, the aerodynamic force is only dependent on the pressure and viscous terms as there is no momentum transfer through the geometry. However, in this study, there is momentum injected through the surface, and therefore, the contribution of the momentum to the overall drag coefficient needs to be considered (see Eq.(4)). Given that the blowing jet is effectively oriented upstream, momentum drag is expected to increase with blowing jet implementation. Consequently, the momentum drag coefficient exhibits a progressive

increase with escalating blowing amplitudes. Nevertheless, the overall drag reduces as the increased momentum drag is compensated by the reduction of pressure and frictional drag.

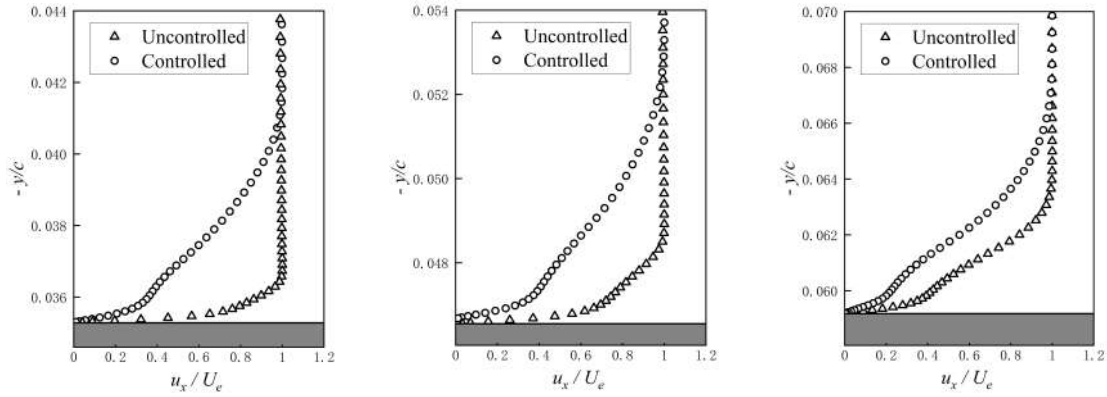

(a) $x/c = 0.05$ (b) $x/c = 0.10$ (c) $x/c = 0.35$

Fig. 14 Mean streamwise velocity profiles on the pressure surface of NACA0012 at (a) $x/c = 0.05$, (b) $x/c = 0.10$ and (c) $x/c = 0.35$. The gray filled region represents the airfoil surface.

D. Engineering Application

The preceding results have shown the impact of the proposed joint control strategy on the NACA0012 airfoil. To further investigate the effectiveness of the joint control in real conditions, the HL-CRM with a mean aerodynamic chord of 7 m is employed as a representative example to examine the robustness of the reported control effect and mechanism in this section. The freestream conditions correspond to a $Re = 5.49 \times 10^6$, $\alpha = 2°$, and temperature of 268 K. Compared with the baseline case in Fig.15(a), the ice prevention at the leading edge is effectively achieved upon the activation of the joint control ($C_\mu = 0.0047$, $A = 0.30$, $h = 5.25\%c$), as illustrated in Fig.15(b). This is caused by the modification of water droplets trajectories after imposing the constant blowing jet control, as analyzed in Section B.

Compared with the baseline case in Fig.16(a), one can observe from Fig.16(b) that the area of the negative pressure zone on the suction side of the HL-CRM expands after applying joint control, aligning with the observations in Section C. The aerodynamic parameters of the HL-CRM with or without joint control are shown in Table 3. A marginal reduction in the lift coefficient is noted, attributed to the generalization of joint control parameters optimized for the NACA0012 airfoil to the HL-CRM configuration. As expected, a notable decrease of 30.6% in the drag coefficient is observed, resulting in a 33.0% improvement in lift-to-drag ratio. Hence, the overall aerodynamic performance of the HL-CRM is significantly improved.

Similar to the efficient control effect on the NACA0012 airfoil introduced in Section A, the joint control also exhibits effects on both anti-icing and drag reduction on the HL-CRM. This test underscores the generalization and effectiveness of the joint control approach across different configurations, illustrating its potential as a robust solution for improving

aerodynamic efficiency and enhancing safety in icing conditions.

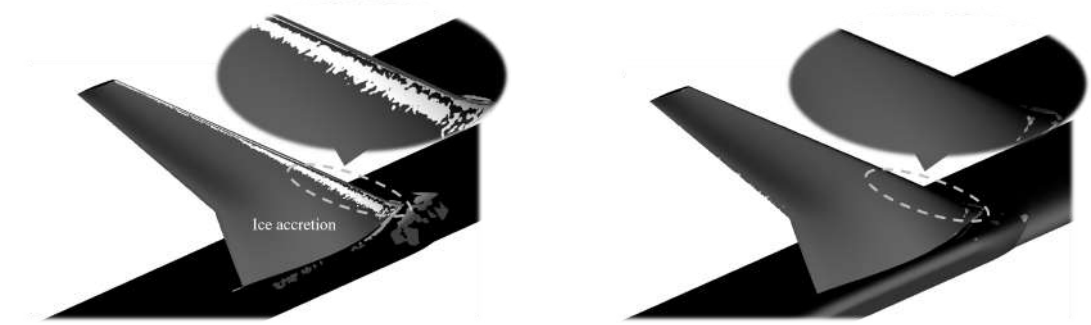

(a) Control off (b) Control on

Fig. 15 Distribution of ice quantified by ice layer thickness on the HL-CRM for the (a) uncontrolled and (b) controlled cases.

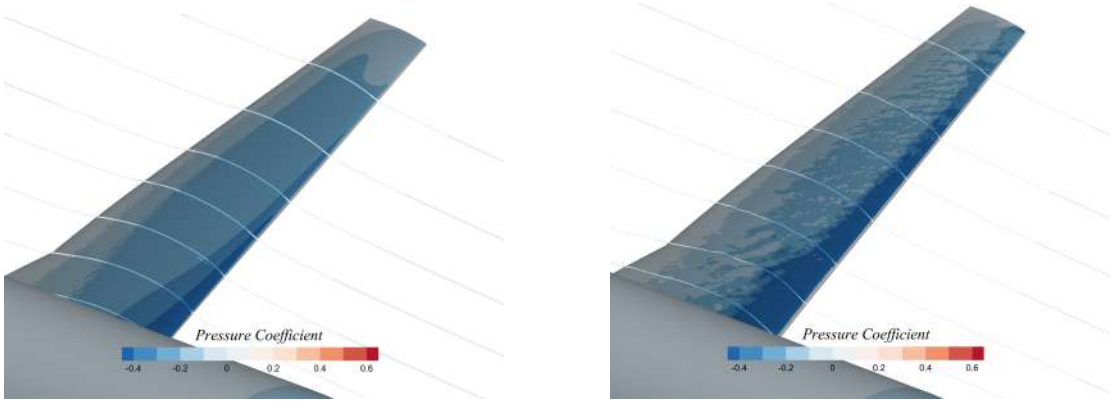

(a) Control off (b) Control on

Fig. 16 Profiles of the pressure coefficient and streamline on the HL-CRM for the (a) uncontrolled and (b) controlled cases.

Table 3 Aerodynamic parameters of the HL-CRM with or without control

CASE	C_L	C_D	C_L/C_D
Control off	0.3170	0.0150	21.13
Control on	0.2924	0.0104	28.11

VI. Conclusion

This work introduced a novel strategy for the joint control of ice prevention and drag reduction by employing the constant blowing jet around the leading edge. Adopting the NACA0012 airfoil as an example, numerical simulations

were carried out to optimize the joint control parameters, including the blowing width and amplitude. After analyzing the control effect on the NACA0012 airfoil and the mechanisms, the control method and parameters were subsequently applied to the HL-CRM. The results indicate that the proposed control method is robust, and it effectively prevents ice formation and enhances aerodynamic performance on the HL-CRM.

After activating the joint control, the inner virtual surface created by the constant blowing control modulates the kinematic parameters of water droplets (i.e., droplet collection efficiency and velocity), blocking droplets from colliding with the wing surface and even freezing to ice. On the other hand, the outer virtual surface redirects the shear created by the blowing and promotes its rolling-up and vortex shedding, which then leads to the formation of a low-pressure core and the reduction of pressure drag. Furthermore, the increased boundary layer thickness persisting downstream on the pressure surface of the airfoil is induced by the blowing jet and consequently contributes to a reduction in skin friction.

From the mechanisms revealed, alternative strategies leading to virtual surfaces would yield comparable control effect. For example, plasma actuation (e.g., DBD plasma actuation) imposed around the leading edge can be another promising option that does not require a continuous supply of blowing air.

Acknowledgments

The authors would like to acknowledge the support from the National Natural Science Foundation of China (Grant Nos. 92152109 and 12202059).

References

[1] Lee, S., and Bragg, M. B., "Investigation of Factors Affecting Iced-Airfoil Aerodynamics," *Journal of Aircraft*, Vol. 40, No. 3, 2003, pp. 499–508. https://doi.org/10.2514/2.3123.

[2] Thomas, S. K., Cassoni, R. P., and MacArthur, C. D., "Aircraft Anti-icing and De-icing Techniques and Modeling," *Journal of Aircraft*, Vol. 33, No. 5, 1996, pp. 841–854. https://doi.org/10.2514/3.47027.

[3] Petty, K., and Floyd, C., "A Statistical Review of Aviation Airframe Icing Accidents in the U.S." *Conference on Aviation, Range, and Aerospace Meteorology*, 2004, pp. 623–628.

[4] Wendeberg, S., "Airport Capacity Effects of Recat or: An Airport View on Recat," *Berlin: WakeNet-3 Europe RECAT Workshop at TU Berlin*, 2011.

[5] Li, H., Waldman, R. M., and Hu, H., "An Experimental Investigation on Unsteady Heat Transfer and Transient Icing Process upon Impingement of Water Droplets," *54th AIAA Aerospace Sciences Meeting*, AIAA Paper 2016-0510, 2016. https://doi.org/10.2514/6.2016-0510.

[6] Drury, M. D., Szefi, J. T., and Palacios, J. L., "Full-Scale Testing of a Centrifugally Powered Pneumatic De-Icing System for Helicopter Rotor Blades," *Journal of Aircraft*, Vol. 54, No. 1, 2017, pp. 220–228. https://doi.org/10.2514/1.C033965.

[7] Chen, N., Hu, Y., Ji, H., and Zhang, M., "Hot-Air Anti-Icing Heat Transfer and Surface Temperature Modeling," *AIAA Journal*, Vol. 59, No. 9, 2021, pp. 3657–3666. https://doi.org/10.2514/1.J059776.

[8] Nagappan, N., Golubev, V., and Nakhla, H., "On Icing Control Using Thermally Activated Synthetic Jets," *51st AIAA Aerospace Sciences Meeting including the New Horizons Forum and Aerospace Exposition*, AIAA Paper 2013-93, 2013. https://doi.org/10.2514/6.2013-93.

[9] Nagappan, N., Golubev, V. V., and Habashi, W., "Parametric Analysis of Icing Control Using Synthetic Jet Actuators," *21st AIAA Computational Fluid Dynamics Conference*, AIAA Paper 2013-2453, 2013. https://doi.org/10.2514/6.2013-2453.

[10] Zhou, W., Liu, Y., Hu, H., Hu, H., and Meng, X., "Utilization of Thermal Effect Induced by Plasma Generation for Aircraft Icing Mitigation," *AIAA Journal*, Vol. 56, No. 3, 2018, pp. 1097–1104. https://doi.org/10.2514/1.J056358.

[11] Yang, S., Yi, X., Guo, Q., Xiao, C., Luo, Z., and Zhou, Y., "Novel Hybrid Ice Protection System Combining Thermoelectric System and Synthetic Jet Actuator," *AIAA Journal*, Vol. 59, No. 4, 2021, pp. 1496–1500. https://doi.org/10.2514/1.J059906.

[12] Shur, M. L., Spalart, P. R., Strelets, M. K., and Travin, A. K., "A Hybrid RANS-LES Approach With Delayed-DES and Wall-modelled LES Capabilities," *International Journal of Heat and Fluid Flow*, Vol. 29, No. 6, 2008, pp. 1638–1649. https://doi.org/https://doi.org/10.1016/j.ijheatfluidflow.2008.07.001.

[13] Doormaal, J. P. V., and Raithby, G. D., "Enhancements of the SIMPLE Method for Predicting Incompressible Fluid Flows," *Numerical Heat Transfer*, Vol. 7, No. 2, 1984, pp. 147–163. https://doi.org/10.1080/01495728408961817.

[14] Leonard, B., "The ULTIMATE Conservative Difference Scheme Applied To Unsteady One-Dimensional Advection," *Computer Methods in Applied Mechanics and Engineering*, Vol. 88, No. 1, 1991, pp. 17–74. https://doi.org/https://doi.org/10.1016/0045-7825(91)90232-U.

[15] Yang, C., Arcondoulis, E. J. G., Yang, Y., Guo, J., Maryami, R., Bi, C., and Liu, Y., "Active Control of Airfoil Turbulent Boundary Layer Noise With Trailing-Edge Blowing," *The Journal of the Acoustical Society of America*, Vol. 153, No. 4, 2023, pp. 2115–2115. https://doi.org/10.1121/10.0017787.

[16] Mao, X., "Sensitivity of Forces To Wall Transpiration In Flow Past An Aerofoil," *Proceedings of the Royal Society of London Series A*, Vol. 471, No. 2184, 2015, p. 20150618. https://doi.org/10.1098/rspa.2015.0618.

[17] Wang, C., Chang, S., and Wu, H., "Lagrangian Approach for Simulating Supercooled Large Droplets's Impingement Effect," *Journal of Aircraft*, Vol. 52, No. 2, 2015, pp. 524–537. https://doi.org/10.2514/1.C032765.

[18] Wirogo, S., and Srirambhatla, S., "An Eulerian Method To Calculate The Collection Efficiency On Two and Three Dimensional Bodies," *41st Aerospace sciences meeting and exhibit*, 2003. https://doi.org/10.2514/6.2003-1073.

[19] Bourgault, Y., Boutanios, Z., and Habashi, W. G., "Three-dimensional Eulerian Approach to Droplet Impingement Simulation Using FENSAP-ICE, Part 1: Model, Algorithm, and Validation," *Journal of aircraft*, Vol. 37, No. 1, 2000, pp. 95–103. https://doi.org/10.2514/2.2566.

[20] Dunham, J., "A Theory of Circulation Control by Slot-blowing, Applied To a Circular Cylinder," *Journal of Fluid Mechanics*, Vol. 33, No. 3, 1968, p. 495–514. https://doi.org/10.1017/S0022112068001473.

[21] Gao, D., Chen, G., Chen, W., Huang, Y., and Li, H., "Active Control of Circular Cylinder Flow With Windward Suction and Leeward Blowing," *Experiments in Fluids*, Vol. 60, 2019, pp. 1–17. https://doi.org/https://doi.org/10.1007/s00348-018-2676-z.

[22] Wu, Z., and Choi, H., "Modification of Flow Behind a Circular Cylinder by Steady and Time-Periodic Blowing," *Physics of Fluids*, Vol. 33, No. 11, 2021, p. 115126. https://doi.org/10.1063/5.0067706.

[23] Vassberg, J., Dehaan, M., Rivers, M., and Wahls, R., "Development of a Common Research Model for Applied CFD Validation Studies," *26th AIAA Applied Aerodynamics Conference*, NO. August, AIAA Paper 2008-6919, 2008. https://doi.org/10.2514/6.2008-6919.

[24] Lacy, D. S., and Sclafani, A. J., "Development of the High Lift Common Research Model (HL-CRM): A Representative High Lift Configuration for Transonic Transports," AIAA Paper 2016-0308, San Diego, California, 2016. https://doi.org/10.2514/6.2016-0308.

[25] "4th AIAA CFD High Lift Prediction Workshop (HLPW-4)," *Committee, AIAA Applied Aerodynamics Technical*, 2022. https://hiliftpw.larc.nasa.gov/index-workshop4.html.

[26] "4th AIAA CFD High Lift Prediction Workshop (HLPW-4)," *Committee, AIAA Applied Aerodynamics Technical*, 2022. https://hiliftpw.larc.nasa.gov/Workshop4/testcases.html.

[27] Huang, L., Huang, P. G., LeBeau, R. P., and Hauser, T., "Numerical Study of Blowing and Suction Control Mechanism on NACA0012 Airfoil," *Journal of Aircraft*, Vol. 41, No. 5, 2004, pp. 1005–1013. https://doi.org/10.2514/1.2255.

[28] Chapin, V. G., and Benard, E., "Active Control of a Stalled Airfoil Through Steady or Unsteady Actuation Jets," *Journal of Fluids Engineering*, Vol. 137, No. 9, 2015, p. 091103. https://doi.org/10.1115/1.4030483.

[29] Harris, C. D., "Two-dimensional aerodynamic characteristics of the NACA 0012 airfoil in the Langley 8 foot transonic pressure tunnel," Tech. rep., NASA TM 81927, 1981.

[30] Sheldahl, R. E., and Klimas, P. C., "Aerodynamic Characteristics of Seven Symmetrical Airfoil Sections Through 180-Degree Angle of Attack for Use In Aerodynamic Analysis of Vertical Axis Wind Turbines," Tech. rep., Sandia National Laboratories, SAND80-2114, 1981. https://doi.org/10.2172/6548367.

[31] Iuliano, E., Brandi, V., Mingione, G., de Nicola, C., and Tognaccini, R., "Water Impingement Prediction on Multi-Element Airfoils by Means of Eulerian and Lagrangian Approach with Viscous and Inviscid Air Flow," *44th AIAA Aerospace Sciences Meeting and Exhibit*, AIAA Paper 2013-2453, 2006, p. 1270. https://doi.org/10.2514/6.2006-1270.

[32] Wahidi, R., and Bridges, D. H., "Effects of Distributed Suction on an Airfoil at Low Reynolds Number," *AIAA Journal*, Vol. 50, No. 3, 2012, pp. 523–539. https://doi.org/10.2514/1.J050913.

[33] Stroh, A., Hasegawa, Y., Schlatter, P., and Frohnapfel, B., "Global Effect of Local Skin Friction Drag Reduction In Spatially Developing Turbulent Boundary Layer," *Journal of Fluid Mechanics*, Vol. 805, 2016, p. 303–321. https://doi.org/10.1017/jfm.2016.545.

[34] Leibovich, S., "Vortex Stability and Breakdown - Survey and Extension," *AIAA Journal*, Vol. 22, No. 9, 1984, pp. 1192–1206. https://doi.org/10.2514/3.8761.

[35] Nair, A. G., Yeh, C.-A., Kaiser, E., Noack, B. R., Brunton, S. L., and Taira, K., "Cluster-Based Feedback Control of Turbulent Post-Stall Separated Flows," *Journal of Fluid Mechanics*, Vol. 875, 2019, p. 345–375. https://doi.org/10.1017/jfm.2019.469.

[36] SU, Z., ZONG, H., LIANG, H., LI, J., XIE, L., LIU, X., KONG, W., and ZHENG, B., "Minimizing Airfoil Drag at Low Angles of Attack With DBD-Based Turbulent Drag Reduction Methods," *Chinese Journal of Aeronautics*, Vol. 36, No. 4, 2023, pp. 104–119. https://doi.org/10.1016/j.cja.2022.11.019.

[37] Vinuesa, R., Bobke, A., Örlü, R., and Schlatter, P., "On Determining Characteristic Length Scales in Pressure-Gradient Turbulent Boundary Layers," *Physics of Fluids*, Vol. 28, No. 5, 2016, p. 055101. https://doi.org/10.1063/1.4947532.

[38] Miura, S., Ohashi, M., Fukagata, K., and Tokugawa, N., "Drag Reduction by Uniform Blowing on the Pressure Surface of an Airfoil," *AIAA Journal*, Vol. 60, No. 4, 2022, pp. 2241–2250. https://doi.org/10.2514/1.J060831.